RSC Advances

PAPER

View Article Online
View Journal | View Issue

Cite this: *RSC Adv.*, 2018, **8**, 32095

Collateral hydrogenation over proton-conducting Ni/$BaZr_{0.85}Y_{0.15}O_{3-\delta}$ catalysts for promoting CO_2 methanation†

Sungjun Choi,[ab] Sung Min Choi,[a] Kyung Joong Yoon,[a] Ji-Won Son,[a] Jong-Ho Lee,[a] Byung-Kook Kim,[a] Byoung-In Sang[b] and Hyoungchul Kim*[a]

Received 23rd July 2018
Accepted 10th September 2018

DOI: 10.1039/c8ra06226a

rsc.li/rsc-advances

Despite the importance of CO_2 methanation for eco-friendly carbon-neutral fuel recycling, the current technologies, relying on catalytic hydrogenation over metal-based catalysts, face technological and economical limitations. Herein, we employ the steam hydrogenation capability of proton conductors to achieve collateral CO_2 methanation over the Ni/$BaZr_{0.85}Y_{0.15}O_{3-\delta}$ catalyst, which is shown to outperform its conventional Ni/Al_2O_3 counterpart in terms of CH_4 yield (8% higher) and long-term stability (3% higher for 150 h) at 400 °C while exhibiting a CH_4 selectivity above 98%. Moreover, infrared and X-ray photoelectron spectroscopy analyses reveal the appearance of distinct mobile proton-related OH bands during the methanation reaction.

Introduction

Global resource depletion and climate change are the most important ecological problems facing humanity at present, being both characterized by "carbon" as a common keyword. The combustion of fossil fuels has upset the natural balance maintained for many thousands of years, with the release of CO_2 leading to climate change, *e.g.*, global warming.[1,2] Carbon neutrality focuses on the environmentally friendly recycling of excessive carbon emissions, providing a paradigm of solving the energy and environmental problems facing mankind.[3,4] Among the technologies of carbon-neutral energy conversion, one of the most important ones is the methanation of CO_2 with H_2, or the Sabatier reaction (best performed at ~400 °C), in which CO_2 and H_2 are exothermically converted to CH_4 and H_2O over a metal catalyst.

$$CO_2\,(g) + 4H_2\,(g) \rightarrow CH_4\,(g) + 2H_2O\,(g), \quad \Delta G_{298\ K} = -113\ kJ\ mol^{-1}, \qquad (1)$$

where G is the Gibbs free energy. Based on the results of studies conducted since the 1910s,[5–17] the abovementioned methanation is most efficiently conducted at ~400 °C using Ni metal-based catalysts (solely responsible for the dissociation of H_2 gas) and Al_2O_3 supports.[6–12,14,17] Recent studies have shown that the partial replacement of Ni with Ru can afford better-performing catalysts.[5,8,9] However, Ni metal-based catalysts suffer from low selectivity and significant deactivation caused by the formation of nickel subcarbonyl species,[5,9] with partial Ru alloying also being inappropriate for commercial applications due to the high cost of the latter metal.[12] Compared to the extensively investigated metal catalysts, which play a key role in the dissociation of H_2 gas, catalyst supports have been relatively underexplored due to the difficulty of utilizing catalytically active oxides at low oxygen partial pressures. Besides, the corresponding studies were merely focused on metal activity (improving reducibility[6,10,14] and electron transfer by the redox couple[17,18]) and/or support effect (increasing metal dispersion,[6,10,13] preventing metal coalescence,[16,18] and improving reactant sorption[7,12,17]) enhancement, not being related to H_2, which is the base material of the hydrogenation reaction. As a result, no new insights into and applications of the catalytic support contribution to CO_2 methanation have been reported.

Herein, we propose a new multi-hydrogenation catalyst for CO_2 methanation comprising Ni metal supported by proton-conductive 15 mol% Y-doped barium zirconate [$BaZr_{0.85}Y_{0.15}O_{3-\delta}$ (BZY)], revealing that the above catalyst surpasses the conventionally used Ni/Al_2O_3 powder in terms of both CH_4 yield (Y_{CH_4}) and formation selectivity (S_{CH_4}, ~100%). Using comprehensive surface analyses based on *in situ* Fourier transform infrared (FT-IR) and X-ray photoelectron spectroscopy (XPS) techniques, we clarify some aspects of mobile proton generation and its effect on CO_2 methanation.

Experimental section

Synthesis and characterization of catalysts

Proton-conducting BZY powder (specific surface area = 12 $m^2\ g^{-1}$) was synthesized by calcining a mixture of $BaCO_3$

[a]*High-Temperature Energy Materials Research Center, Korea Institute of Science and Technology, 5 Hwarang-ro 14-gil, Seongbuk-gu, Seoul 02792, Republic of Korea. E-mail: hyoungchul@kist.re.kr*

[b]*Department of Chemical Engineering, Hanyang University, 222 Wangsimni-ro, Seongdong-gu, Seoul 04763, Republic of Korea*

† Electronic supplementary information (ESI) available. See DOI: 10.1039/c8ra06226a

(Cerac), ZrO_2 (Junsei), and Y_2O_3 (High Purity Chemicals) powders with the desired stoichiometric ratio at 1300 °C for 2 h, with detailed information provided in our previous paper.[19,20] Spherical Al_2O_3 powder (Alfa Aesar, specific surface area = 28 $m^2\ g^{-1}$) was chosen as an inert support for comparison. $Ni(NO_3)_2 \cdot 6H_2O$ (Sigma-Aldrich) was used as a metal precursor. Ni-loaded catalysts (Ni/BZY and Ni/Al_2O_3) were prepared using a deposition–precipitation method followed by freeze-drying, and the obtained powders were calcined in an electric box furnace for 3 h at 600 and 400 °C, respectively. The crystal structures and morphologies of powders were examined by X-ray diffraction (XRD, D/Max-2500, Rigaku; Cu Kα) and transmission electron microscopy (TEM, Talos F200X, FEI; 200 kV) analyses. All diffraction patterns were obtained in the 2θ range of 20–80° with a scan step of 0.01° and a scan rate of 1° min^{-1}. The specimens for TEM were prepared by dispersing the catalyst powder in ethanol and then drop-casting the solution onto a porous carbon film supported on a Cu grid. Before the installation of sample grid, it held on 10 minutes to evaporate liquid ethanol.

CO_2 methanation tests of catalysts

All catalytic activity tests were performed using a gas chromatograph (7890B, Agilent) and an atmospheric-pressure fixed-bed tubular reactor. Typically, a 0.1 g powder sample was placed in the middle of the reactor held inside a tube furnace. The reactant gases were pre-mixed in the condition of $H_2 : CO_2 : Ar = 4 : 1 : 5$, and the total feed flow rate was maintained at 100 mL min^{-1}. Prior to being utilized in the methanation reaction, all catalysts were reduced by 10 mol% H_2 gas balanced in Ar at 600 °C for 2 h, and their catalytic activities were evaluated in terms of Y_{CH_4}, S_{CH_4}, X_{CO_2}, and X_{H_2}:

$$Y_{CH_4} = \frac{[\text{moles of } CH_4 \text{ produced}]}{[\text{moles of } CO_2 \text{ fed}]} \times 100, \quad (2)$$

$$S_{CH_4} = \frac{[\text{moles of } CH_4 \text{ produced}]}{[\text{moles of } CO_2 \text{ converted}]} \times 100. \quad (3)$$

$$X_i = \frac{[\text{moles of i converted}]}{[\text{moles of i fed}]} \times 100 \quad (i = CO_2, H_2). \quad (4)$$

Surface analyses of catalysts

In situ FT-IR spectra were recorded using a corresponding spectrometer (Nicolet 6700, Thermo Scientific) and a controlled atmospheric chamber (DiffusIR, PIKE Technologies) used to react the pre-mixed gases ($H_2 : CO_2 : He = 4 : 1 : 5$, total flow rate = 100 mL min^{-1}). Additional technical details of the above FT-IR system can be found elsewhere.[21] To stabilize the

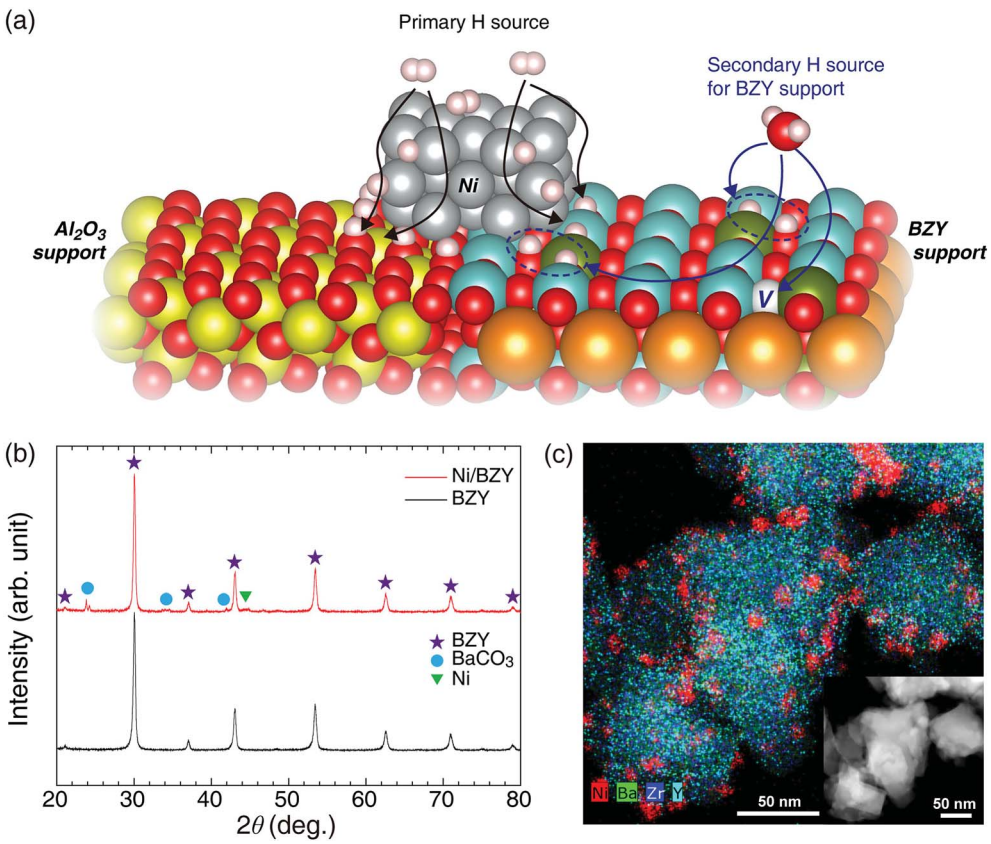

Fig. 1 (a) Schematic illustration of different hydrogenation processes occurring on Ni/BZY (right) and Ni/Al_2O_3 (left) surfaces. (b) XRD patterns of as-prepared BZY support and the Ni/BZY catalyst. (c) TEM and EDS mapping images of as-prepared Ni/BZY, with Ni, Ba, Zr, and Y elements indicated by red, green, blue, and cyan colors, respectively.

temperature of the reaction chamber up to 400 °C, we used He gas, which is an inert gas with the highest thermal conductivity. XPS (PHI 5000 VerasProbe, Ulvac-PHI) analyses were performed using monochromatic Al Kα (1486.6 eV) radiation, and spectral deconvolution was conducted through Gaussian–Lorentzian functions considering the chemistry of the powders.

Results and discussion

Proton-conductive ceramics are oxide-based inorganic materials capable of rapid proton transfer due to facilitating the dissociative adsorption of H_2O *via* utilization of oxygen vacancies at 350–600 °C,[22–24] with the best known examples including perovskites such as doped alkaline-earth cerates and zirconates. Based on the results of various studies conducted on electrolyte materials for low-temperature solid-oxide fuel cells,[20,25] we concluded that the proton conduction process and the Sabatier reaction feature high similarity and compatibility. First, both of the above processes rely on a hydrogenation step for proton utilization. Second, in the temperature range of the Sabatier reaction, sufficient proton incorporation and conductivity are observed. Finally, both reactions take place in similar wet atmospheres. Considering that proton-conductive oxides adsorb H_2O molecules to generate two mobile protons with hydroxyl group,[22,23] we expected these functional supports to facilitate CO_2 methanation by introducing a new hydrogenation reaction, as shown in Fig. 1(a). In previously reported studies on CO_2 hydrogenation involving the Ni metal and Al_2O_3 support, the reaction mechanism was suggested with a formate ($HCOO^-$) intermediate.[12,21] The adsorbed CO on the catalyst is converted to CH_4 due to hydrogen concentration and thermodynamic favorability at the transition state.[21,26,27] In this step, sufficient hydrogenation process is very important to produce the target CH_4 and to suppress the CO side reactions. Thus, in contrast to the inert Al_2O_3 support, BZY provides an additional hydrogenation pathway for CO_2 methanation, along with the main one occurring on Ni metal, which results in the improvement of the overall reaction capacity.

As shown in Fig. 1(b) and (c), the BZY support, one of the most reliable highly proton-conductive materials, was herein used to prepare a novel CO_2 methanation catalyst. Fig. 1(b) presents the XRD patterns of the BZY support and 5 wt% Ni/BZY catalyst powders, revealing that the former pattern featured only a single perovskite ($BaZrO_3$) phase and no secondary phases, whereas an additional Ni metal peak (at 44.5°) was observed for Ni/BZY, indicating that Ni was well compatible with the BZY support. Note that although $BaCO_3$ peaks (at 23.9, 24.3, 34.6, and 42.0°) were detected in the XRD spectra of Ni/BZY prepared *via* urea hydrolysis, the effects of the above compounds on the overall CO_2 methanation reaction were negligible (for both BZY and $BaCO_3$/BZY, $Y_{CH_4} = 0$ at 400 °C; Fig. S1†). Fig. 1(c) shows the TEM and energy dispersive X-ray spectroscopy (EDS) images of as-prepared Ni/BZY powder, with the homogeneous distribution of BZY constituent elements indicating that no secondary phase was present in the as-prepared single-phase BZY, as confirmed by XRD results. Moreover, the BZY surface featured well distributed spherical Ni nanoparticles with an average diameter of ~10.68 nm (standard deviation = 2.64 nm). ESI XRD and TEM data for comparison

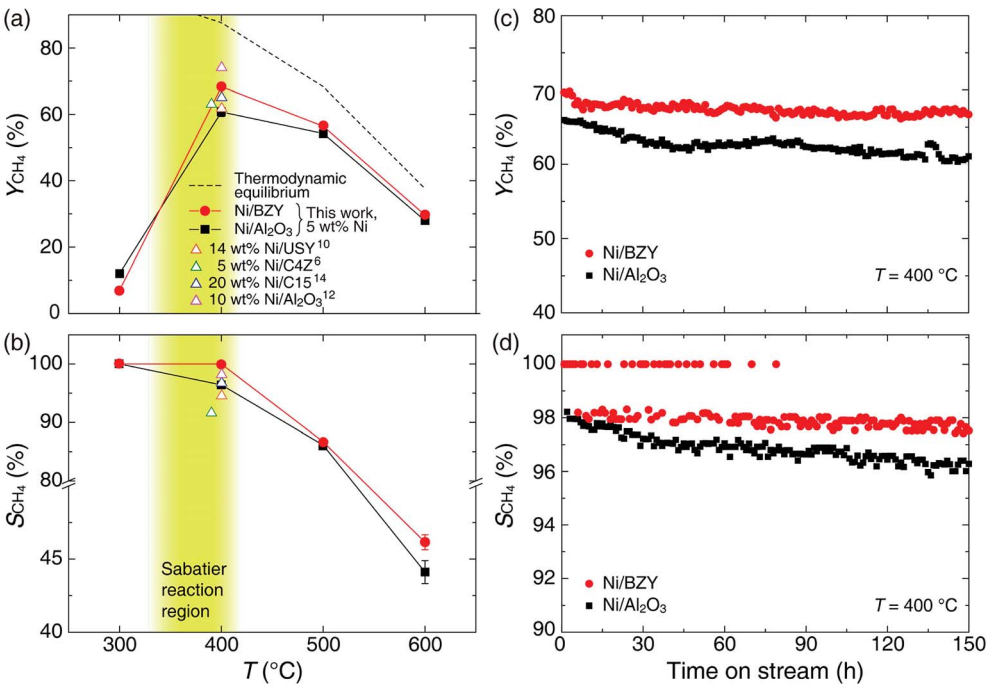

Fig. 2 Temperature-dependent (a) Y_{CH_4} and (b) S_{CH_4} values of Ni/BZY and Ni/Al_2O_3. The dashed line represents the thermodynamic equilibrium performance of Y_{CH_4} under the chosen experimental conditions ($H_2/CO_2 = 4.0$). The yellow-green-colored area corresponds to the temperature range of the Sabatier reaction. USY, C4Z, and C15 denote ultra-stable Y zeolite, $Ce_{0.8}Zr_{0.2}O_2$, and composite supports (55% γ-Al_2O_3 and 15% equivalent loading of ZrO_2, TiO_2, CeO_2), respectively. Long-term stability test of Ni/BZY and Ni/Al_2O_3 performed at $H_2/CO_2 = 4.0$ and 400 °C: (c) Y_{CH_4} and (d) S_{CH_4}.

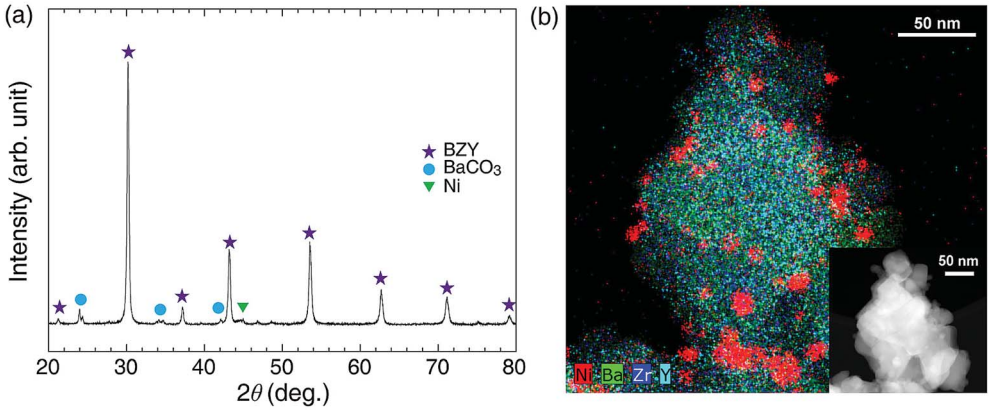

Fig. 3 XRD pattern (a) and TEM-EDS images (b) of Ni/BZY subjected to 150 h CO_2 methanation at 400 °C. The average particle diameter of Ni on the BZY support equaled ~11.50 nm (standard deviation = 4.04 nm). The red, green, blue, and cyan colors correspond to the elements Ni, Ba, Zr, and Y, respectively.

samples (Al_2O_3 support and Ni/Al_2O_3 powders) are provided in Fig. S2.†

As is well known, low operating temperatures are desirable for achieving higher Y_{CH_4} and S_{CH_4}, since the Sabatier reaction is thermodynamic equilibrium-limited.[15] Fig. 2(a) and (b) shows the temperature-dependent Y_{CH_4} and S_{CH_4} values of Ni/BZY and Ni/Al_2O_3 obtained by gas chromatography analysis of reaction products formed in a fixed-bed tubular reactor, revealing that Ni/BZY achieved a maximum $Y_{CH_4} = 68.33\%$ at 400 °C, while the conventional Ni/Al_2O_3 featured a smaller value of $Y_{CH_4} = 60.76\%$. Assuming that hydrogenation of Ni metal in the Ni/Al_2O_3 catalyst is the only hydrogen source, the increase in Y_{CH_4} at Ni/BZY is the results of new hydrogenation pathway by BZY support (about 12% of Y_{CH_4}). Thus, the Ni/BZY system described herein achieved a substantially higher Y_{CH_4} than previously reported catalysts (only Ni metal and $H_2/CO_2 \sim 4$ gas conditions

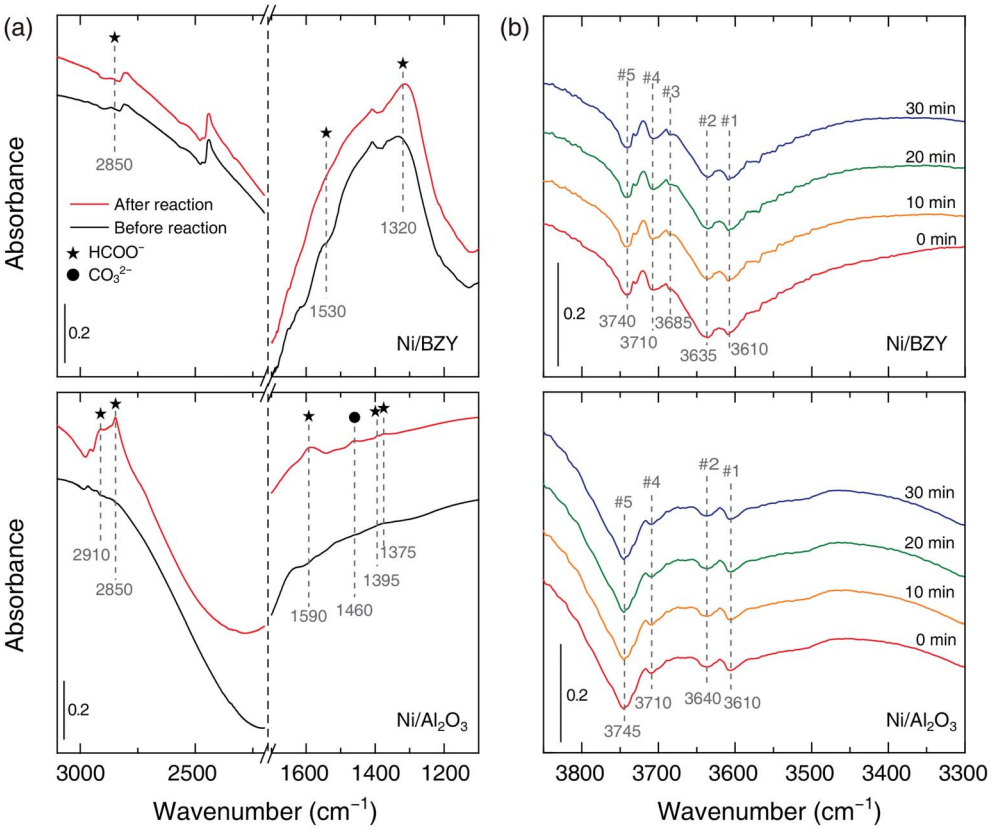

Fig. 4 *In situ* FT-IR spectra of species adsorbed on Ni/BZY and Ni/Al_2O_3 during CO_2 methanation at 400 °C. (a) Analysis of formate (star) and carbonate (filled circle) species before/after CO_2 methanation. (b) Time-dependent analysis of OH groups contained in the flowing reactant gases at 400 °C. Red, yellow, green, and blue lines correspond to time steps of 0, 10, 20, and 30 min, respectively.

are considered).[6,10,12,14] The progress of CO_2 methanation was gradually suppressed with increasing temperature due to the reverse water-gas shift (RWGS) reaction becoming thermodynamically dominant at $T > 400$ °C. In addition, Ni/BZY and Ni/Al_2O_3 exhibited different S_{CH_4} behavior, *i.e.*, the former system attained $S_{CH_4} = 100\%$, while the latter one achieved a relatively low S_{CH_4} of 96.43% due to the production of CO gas by the RWGS reaction.[15] ESI data of X_{CO_2} and X_{H_2} are also provided in Fig. S3.† The Ni/BZY catalyst showed higher performance than the Ni/Al_2O_3 catalyst: about 3.84% and 6.62% X_{CO_2} and X_{H_2}, respectively. To investigate the long-term stability of both catalysts, we subjected them to 150 h CO_2 methanation exposure at 400 °C, with the obtained results shown in Fig. 2(c) and (d). After 150 h, the Y_{CH_4} of Ni/BZY was reduced by ~4% compared to the initial value, while that of Ni/Al_2O_3 was reduced by ~7%. However, the corresponding long-term selectivity changes were more noticeable, *i.e.*, for Ni/Al_2O_3, S_{CH_4} gradually decreased to 96% of the original value after 150 h, whereas Ni/BZY maintained $S_{CH_4} \approx 100\%$ during the first 79 h, finally reaching $S_{CH_4} = 98\%$ after 150 h.

As shown in Fig. 3, XRD and TEM-EDS analyses of Ni/BZY catalysts subjected to 150 h exposure to CO_2 methanation conditions demonstrated that no noticeable carbon deposition occurred, with performance degradation ascribed to the slight coarsening of Ni metal nanoparticles (~1 nm diameter increase). ESI XRD and TEM data of a comparison sample (Ni/Al_2O_3 powders after 150 h CO_2 methanation) are also provided in Fig. S4.† Combining the above results, we concluded that the CO_2 methanation performance was significantly influenced by the proton conductivity of the support.

The role of the catalyst support was investigated by *in situ* FT-IR characterization of species adsorbed on the catalyst surface during methanation. Fig. 4(a) shows that the common IR bands at 2910–2850 and 1590–1320 cm^{-1} appearing in adsorbate spectra before and after the reaction can be ascribed to formate,[21] which is suggested to be the main intermediate of CO_2 methanation regardless of the support material. However, carbonate (CO_3^{2-}, 1460 cm^{-1}) was also observed on the surface of the Ni/Al_2O_3 catalyst after the reaction, suggesting that CO generation (resulting in lower S_{CH_4}) could be ascribed to a side reaction of the above species. Fig. 4(b) shows the time-dependent evolution of OH bands in the CO_2 methanation mixture obtained using Ni/BZY and Ni/Al_2O_3 catalysts at 400 °C. Notably, four OH bands (#1, 2, 4, 5) at 3750–3600 cm^{-1} were observed for Ni/Al_2O_3, while a total of five OH bands (#1, 2, 3, 4, 5) were observed for Ni/BZY. As reported in literature,[16,17] multiple OH bands are observed for Ni-loaded catalysts due to their use resulting in sufficient hydrogenation. Specifically, band #5 observed for all catalysts containing Ni metal was attributed to the hydroxyl moieties of the reaction sites generated at the Ni metal/support interface. In addition, it is well-known that low-wavenumber bands with low binding energies can be considered to have a multi-fold bond,[28] *i.e.*, a bond of a single OH species on the surface bound to a number of metal atoms. From the viewpoint of such reaction energy, band #5, exhibiting the largest wavenumber among the five OH bands, corresponded to species having the smallest number of surface bonds and thus most actively contributing to CO_2 methanation. Therefore, the observation of the above band in the case of both Ni/BZY and Ni/Al_2O_3 was ascribed to the significant CO_2 methanation progress achieved by these catalysts. However, Ni/BZY and Ni/Al_2O_3 could be discriminated by the presence/absence of the #3 band, which seemed to reflect the role of the proton-conductive support.

To confirm that hydrogenation process differences reflect the different roles of the proton-conductive support, we performed *in situ* FT-IR analysis during slow hydrogenation on the pure support. As shown in Fig. 4(b) and 5, the #3 band gained intensity with time in the case of the BZY support, in clear contrast to the results obtained for Al_2O_3, which allowed us to conclude that the above band corresponded to mobile protons produced due to the proton-conducting capability of BZY. Moreover, the additional OH production pathway was expected to facilitate CO_2 methanation on Ni/BZY catalysts. Therefore, the difference of CO_2 methanation performance between the two catalysts originated from the presence/absence of mobile protons, *i.e.*, was related to the occurrence

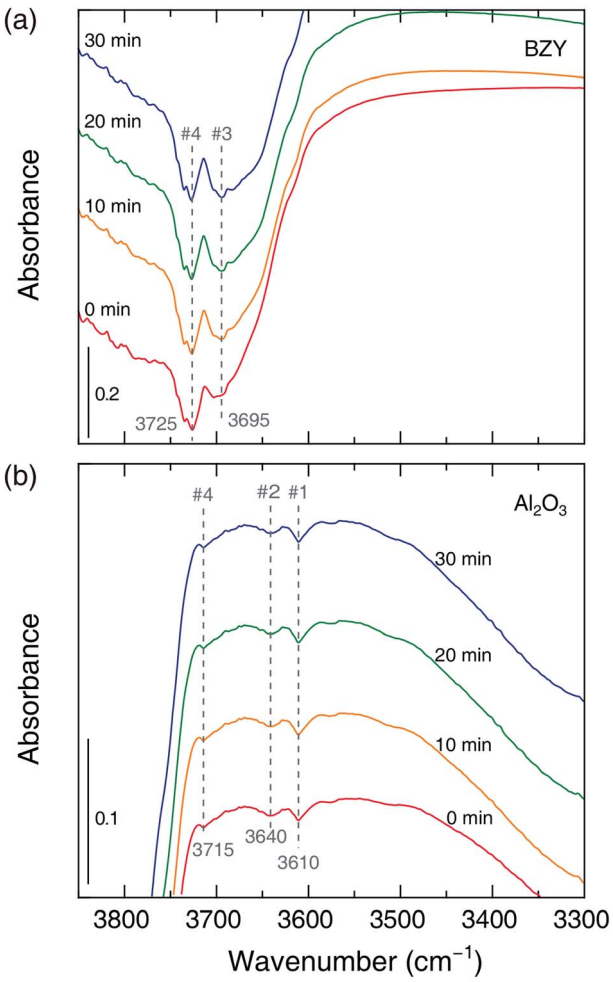

Fig. 5 Time-dependent FT-IR spectra of OH groups recorded under the conditions of reactant gas flow at 400 °C [(a): BZY, (b): Al_2O_3]. Red, yellow, green, and blue lines correspond to times of 0, 10, 20, and 30 min, respectively.

of additional hydrogenation processes on the proton-conducting support.

Tangible evidence of OH group formation from mobile protons on the BZY surface was provided by the O 1s XPS spectra of Ni/BZY (see Fig. 6). The peak centered at ~528.5 eV was assigned to the lattice oxygen of BZY,[29–31] whereas those at ~531.5 and ~533 eV were ascribed to weakly adsorbed H_2O and adsorbed carbon-containing species such as $BaCO_3$ and formate, respectively.[32,33] Interestingly, the peak at ~530.5 eV gained intensity with progressing CO_2 methanation, thus probably corresponding to the surface hydroxyl groups associated with the mobile proton.[33] In order to clarify the characteristics of OH groups in the XPS spectra of the proton-conductive support, Ni/Al_2O_3 was subjected to XPS analysis for comparison, with the results shown in Fig. S5.† In the above XPS spectra, the peak of Al–O bond lattice oxygen appeared at ~531 eV, and ignorable OH peaks were observed, in agreement with the results of O 1s XPS analysis of conventional Al_2O_3 reported in a number of documents.[34–36] Thus, the decreased amount of OH species observed for Ni/Al_2O_3 was in stark contrast to the large number of hydroxyl species observed on the surface of Ni/BZY under identical conditions. Thus, the proton-conductive BZY support clearly provided an alternative hydrogenation path, which improved the performance of Ni/BZY in the CO_2 methanation reaction.

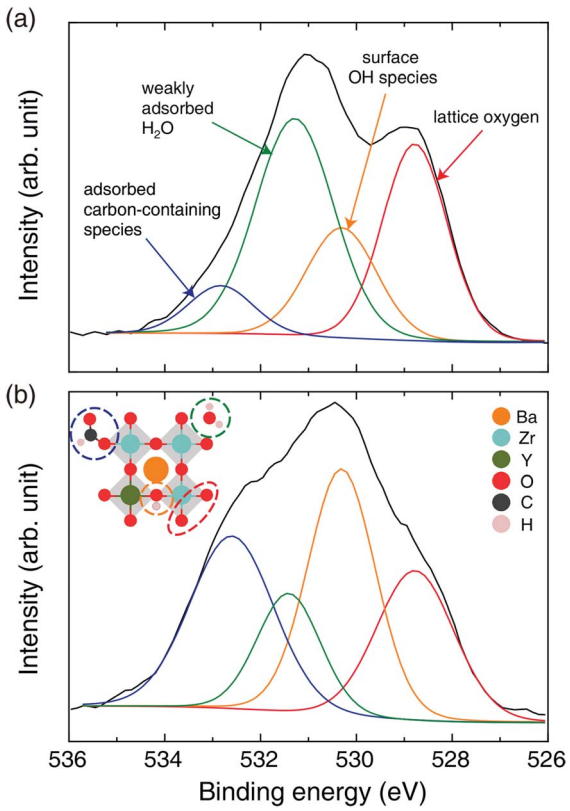

Fig. 6 O 1s core level XPS spectra of Ni/BZY (a) before and (b) after methanation. Red, yellow, green, and blue lines correspond to lattice oxygen, surface OH species, weakly adsorbed H_2O, and adsorbed carbon-containing species (contaminant, $BaCO_3$ and formate), respectively.

Conclusions

In summary, we successfully demonstrated that the CO_2 methanation performance of supported metal catalysts can be improved by collateral hydrogenation over a proton-conductive support. Since the proton-conductive BZY can incorporate H_2O molecules and generate mobile protons in a wet atmosphere at 350–600 °C, the formation of mobile protons on this oxide support can provide an additional hydrogen source and influence the CO_2 hydrogenation mechanism. Thus, Ni/BZY showed an 8% higher CH_4 yield at 400 °C and a 3% higher long-term stability over 150 h than Ni/Al_2O_3. Interestingly, the distinct time-dependent FT-IR band of hydroxyl groups corresponding to mobile protons was only observed for BZY. In addition, according to XPS results, the amount of surface OH species increased during CO_2 methanation, evidencing the generation of mobile protons in the proton-conductive support. Such understanding and exploitation of proton-conductive supports is expected to improve the performance of eco-friendly carbon-neutral CO_2 methanation reactions and enhance their industrial applicability.

Conflicts of interest

There are no conflicts to declare.

Acknowledgements

This work was conducted under the Global Frontier R&D Program on Center for Multiscale Energy Systems (Grant No. NRF-2015M3A6A7065442) the National Research Foundation (NRF) of Korea funded by the Ministry of Science and ICT, Republic of Korea. This work also supported in part by the Institutional Research Program of the Korea Institute of Science and Technology (2E28040).

References

1 G. A. Florides and P. Christodoulides, *Environ. Int.*, 2009, **35**, 390–401.
2 D. Mattia, M. D. Jones, J. P. O'Byrne, O. G. Griffiths, R. E. Owen, E. Sackville, M. McManus and P. Plucinski, *ChemSusChem*, 2015, **8**, 4064–4072.
3 S. De, J. Zhang, R. Luque and N. Yan, *Energy Environ. Sci.*, 2016, **9**, 3314–3347.
4 N. Yan and K. Philippot, *Curr. Opin. Chem. Eng.*, 2018, **20**, 86–92.
5 D. J. Elliott and J. H. Lunsford, *J. Catal.*, 1979, **57**, 11–26.
6 W. Cai, Q. Zhong and Y. Zhao, *Catal. Commun.*, 2013, **39**, 30–34.
7 A. Borgschulte, N. Gallandat, B. Probst, R. Suter, E. Callini, D. Ferri, Y. Arroyo, R. Erni, H. Geerlings and A. Zuttel, *Phys. Chem. Chem. Phys.*, 2013, **15**, 9620–9625.
8 S. Hwang, J. Lee, U. G. Hong, J. H. Baik, D. J. Koh, H. Lim and I. K. Song, *J. Ind. Eng. Chem.*, 2013, **19**, 698–703.
9 W. Zhen, B. Li, G. Lu and J. Ma, *RSC Adv.*, 2014, **4**, 16472–16479.

10 I. Graça, L. V. González, M. C. Bacariza, A. Fernandes, C. Henriques, J. M. Lopes and M. F. Ribeiro, *Appl. Catal., B*, 2014, **147**, 101–110.
11 G. Garbarino, D. Bellotti, P. Riani, L. Magistri and G. Busca, *Int. J. Hydrogen Energy*, 2015, **40**, 9171–9182.
12 H. Muroyama, Y. Tsuda, T. Asakoshi, H. Masitah, T. Okanishi, T. Matsui and K. Eguchi, *J. Catal.*, 2016, **343**, 178–184.
13 H. H. Shin, L. Lu, Z. Yang, C. J. Kiely and S. McIntosh, *ACS Catal.*, 2016, **6**, 2811–2818.
14 S. Abate, C. Mebrahtu, E. Giglio, F. Deorsola, S. Bensaid, S. Perathoner, R. Pirone and G. Centi, *Ind. Eng. Chem. Res.*, 2016, **55**, 4451–4460.
15 X. Su, J. Xu, B. Liang, H. Duan, B. Hou and Y. Huang, *J. Energy Chem.*, 2016, **25**, 553–565.
16 J. Xu, X. Su, H. Duan, B. Hou, Q. Lin, X. Liu, X. Pan, G. Pei, H. Geng, Y. Huang and T. Zhang, *J. Catal.*, 2016, **333**, 227–237.
17 J. A. H. Dreyer, P. Li, L. Zhang, G. K. Beh, R. Zhang, P. H. L. Sit and W. Y. Teoh, *Appl. Catal., B*, 2017, **219**, 715–726.
18 Y. Zeng, H. Ma, H. Zhang, W. Ying and D. Fang, *Fuel*, 2014, **137**, 155–163.
19 S. M. Choi, J.-H. Lee, J. Hong, H. Kim, K. J. Yoon, B.-K. Kim and J.-H. Lee, *Int. J. Hydrogen Energy*, 2014, **39**, 7100–7108.
20 S. M. Choi, J.-H. Lee, J. Hong, K. J. Yoon, J.-W. Son, B.-K. Kim, H.-W. Lee and J.-H. Lee, *J. Power Sources*, 2016, **332**, 299–304.
21 S. Choi, B.-I. Sang, J. Hong, K. J. Yoon, J.-W. Son, J.-H. Lee, B.-K. Kim and H. Kim, *Sci. Rep.*, 2017, **7**, 41207.
22 Y. Yamazaki, P. Babilo and S. M. Haile, *Chem. Mater.*, 2008, **20**, 6352–6357.
23 E. Fabbri, D. Pergolesi and E. Traversa, *Chem. Soc. Rev.*, 2010, **39**, 4355–4369.
24 J.-S. Kim and Y.-C. Kim, *Solid State Ionics*, 2017, **306**, 137–141.
25 K. Bae, D. Y. Jang, H. J. Choi, D. Kim, J. Hong, B.-K. Kim, J.-H. Lee, J.-W. Son and J. H. Shim, *Nat. Commun.*, 2017, **8**, 14553.
26 D. E. Peebles, D. W. Goodman and J. M. White, *J. Phys. Chem.*, 1983, **87**, 4378–4387.
27 A. Beuls, C. Swalus, M. Jacquemin, G. Heyen, A. Karelovic and P. Ruiz, *Appl. Catal., B*, 2012, **113–114**, 2–10.
28 C. Binet, M. Daturi and J.-C. Lavalley, *Catal. Today*, 1999, **50**, 207–225.
29 W. Sun, M. Liu and W. Liu, *Adv. Energy Mater.*, 2013, **3**, 1041–1050.
30 W. Sun, Z. Shi, M. Liu, L. Bi and W. Liu, *Adv. Funct. Mater.*, 2014, **24**, 5695–5702.
31 C. Aruta, C. Han, S. Zhou, C. Cantoni, N. Yang, A. Tebano, T.-L. Lee, C. Schlueter and A. Bongiorno, *J. Phys. Chem. C*, 2016, **120**, 8387–8391.
32 D. Jampaiah, K. M. Tur, S. J. Ippolito, Y. M. Sabri, J. Tardio, S. K. Bhargava and B. M. Reddy, *RSC Adv.*, 2013, **3**, 12963–12974.
33 P. Venkataswamy, D. Jampaiah, K. N. Rao and B. M. Reddy, *Appl. Catal., A*, 2014, **488**, 1–10.
34 B. V. Crist, *Handbooks of Monochromatic XPS Spectra – 5 Volume Series*, XPS International LLC, CA, 2005.
35 J. Peng, Q. Sun, Z. Zhai, J. Yuan, X. Huang, Z. Jin, K. Li, S. Wang, H. Wang and W. Ma, *Nanotechnology*, 2013, **24**, 484010.
36 A. Celebioglu, S. Vempati, C. Ozgit-Akgun, N. Biyikli and T. Uyar, *RSC Adv.*, 2014, **4**, 61698–61705.